# The Far-Infrared Surveyor (FIS) for AKARI*

Mitsunobu Kawada,[1] Hajime Baba,[2] Peter D. Barthel,[3] David Clements,[4] Martin Cohen,[5] Yasuo Doi,[6] Elysandra Figueredo,[7] Mikio Fujiwara,[8] Tomotsugu Goto,[2] Sunao Hasegawa,[2] Yasunori Hibi,[9] Takanori Hirao,[1 †] Norihisa Hiromoto,[10] Woong-Seob Jeong,[2] Hidehiro Kaneda,[2] Toshihide Kawai,[11] Akiko Kawamura,[1] Do Kester,[12] Tsuneo Kii,[2] Hisato Kobayashi,[2,13] Suk Minn Kwon,[14] Hyung Mok Lee,[15] Sin'itirou Makiuti,[2] Hiroshi Matsuo,[9] Shuji Matsuura,[2] Thomas G. Müller,[16] Noriko Murakami,[1] Hirohisa Nagata,[2] Takao Nakagawa,[2] Masanao Narita,[2] Manabu Noda,[17] Sang Hoon Oh,[15] Yoko Okada,[2] Haruyuki Okuda,[2] Sebastian Oliver,[18] Takafumi Ootsubo,[1] Soojong Pak,[19] Yong-Sun Park,[15] Chris P. Pearson,[2,20] Michael Rowan-Robinson,[4] Toshinobu Saito,[2,13] Alberto Salama,[20] Shinji Sato,[1] Richard S. Savage,[18] Stephen Serjeant,[7] Hiroshi Shibai,[1] Mai Shirahata,[2] Jungjoo Sohn,[15] Toyoaki Suzuki,[2,13] Toshinobu Takagi,[2] Hidenori Takahashi,[21] Matthew Thomson,[18] Fumihiko Usui,[2] Eva Verdugo,[20] Toyoki Watabe,[11] Glenn J. White,[7,22] Lingyu Wang,[4] Issei Yamamura,[2] Chisato Yamamuchi,[2] and Akiko Yasuda[2,23]

*kawada@u.phys.nagoya-u.ac.jp*

[1] *Graduate School of Sciences, Nagoya University, Furo-cho, Chikusa-ku, Nagoya 464-8602, Japan*

[2] *Institute of Space and Astronautical Science, JAXA, 3-1-1 Yoshinodai, Sagamihara 229-8510, Japan*

[3] *Groningen Kapteyn Institute, Rijksuniversiteit, Landleven 12, Postbus 800, 9700 AV Groningen, Netherlands*

[4] *Imperial College, London, Blackett Laboratory, Prince Consort Road, London, SW7 2AZ, UK*

[5] *Radio Astronomy Laboratory, 601 Campbell Hall, University of California, Berkeley, CA94720, USA*

[6] *Department of General System Studies, Graduate School of Arts and Sciences, The University of Tokyo, 3-8-1 Komaba, Meguro-ku, Tokyo 153-8902, Japan*

[7] *Department of Physics and Astronomy, Faculty of Science, The Open University, Walton Hall, Milton Keynes, MK7 6AA, UK*

[8] *Advanced Communications Technology Group, New Generation Network Research Center, NICT, 4-2-1 Nukui-Kitamachi, Koganei, Tokyo 184-8795, Japan*

[9] *Advanced Technology Center, National Astronomical Observatory of Japan, 2-21-1 Osawa, Mitaka, Tokyo 181-8588, Japan*

[10] *Optelectronics and Electromagnetic Wave Engineering, Shizuoka University, 3-5-1 Johoku, Hamamatsu, Japan*

[11] *Technical Center of Nagoya University, Furo-cho, Chikusa-ku, Nagoya 464-8601, Japan*

[12] *Netherlands Institute for Space Reasearch SRON, Landleven 12, PO Box 800, 9700 AV Groningen,*

*Netherlands*

[13] *Department of Physics, Graduate School of Science, The University of Tokyo, Bunkyo-ku, Tokyo 113-0033, Japan*

[14] *Department of Science Education, Kangwon National University, 192-1 Hyoja-Dong, Chuncheon, Gangwon-Do, 200-701, Korea*

[15] *Astronomy Program, Department of Physics and Astronomy, FPRD, Seoul National University, Shillim-dong, Kwanak-gu, Seoul 151-742, Korea*

[16] *Max-Planck-Institut für extraterrestrische Physik, Giessenbachstrasse, 85748 Garching, Germany*

[17] *Nagoya City Science Museum, 2-17-1 Sakae, Naka-ku, Nagoya 460-0008, Japan*

[18] *Astronomy Centre, University of Sussex, Falmer, Brighton, BN1 9QJ, UK*

[19] *Department of Astronomy and Space Science, Kyung Hee University, Yongin-si, Gyeonggi-do 446-701, Korea*

[20] *European Space Astronomy Centre, ESA, Villanueva de la Canada, Post Box 78, 28691 Madrid, Spain*

[21] *Gunma Astronomical Observatory, 6860-86 Nakayama, Takayama-mura, Agatsuma-gun, Gunma 377-0702, Japan*

[22] *Space Science and Technology Division, The Rutherford Appleton Laboratory, Chilton, Didcot, Oxfordshire OX11 0QX, England*

[23] *The Graduate University for Advanced Studies, Shonan Village, Hayama, Kanagawa 240-0193, Japan*

(Received 2007 0; accepted 2007 0)

## Abstract

The Far-Infrared Surveyor (FIS) is one of two focal plane instruments on the AKARI satellite. FIS has four photometric bands at 65, 90, 140, and 160 $\mu$m, and uses two kinds of array detectors. The FIS arrays and optics are designed to sweep the sky with high spatial resolution and redundancy. The actual scan width is more than eight arcmin, and the pixel pitch is matches the diffraction limit of the telescope. Derived point spread functions (PSFs) from observations of asteroids are similar to the optical model. Significant excesses, however, are clearly seen around tails of the PSFs, whose contributions are about 30% of the total power. All FIS functions are operating well in orbit, and its performance meets the laboratory characterizations, except for the two longer wavelength bands, which are not performing as well as characterized. Furthermore, the FIS has a spectroscopic capability using a Fourier transform spectrometer (FTS). Because the FTS takes advantage of the optics and detectors of the photometer, it can simultaneously make a spectral map. This paper summarizes the in-flight technical and operational performance of the FIS.

**Key words:** infrared: general–instrumentation: detectors–vehicles: instruments

## 1. Introduction

The first extensive survey of the far-infrared sky was made by the *Infrared Astronomy Satellite* (IRAS) launched in 1983, more than two decades ago. IRAS provided point source catalogs, as well as infrared sky maps, for almost the entire sky, revealing the infrared view of the universe. The IRAS products became a standard dataset, not only for infrared astronomy but also for many other fields. With the widespread use of the IRAS dataset, observations in the infrared are now considered an irreplaceable tool. Compared with the datasets at other wavelengths, the IRAS dataset appears rather shallow, although it provides an unbiased and wide area coverage survey. However, a next-generation infrared dataset is needed to push the frontier of astrophysics. The Far-Infrared Surveyor (FIS) on the AKARI satellite (Shibai H. 2007a; Murakami et al. 2007) was developed to provide this new dataset in the far-infrared region, taking advantage of recent technology, including the cryogenics (Nakagawa et al. 2007). The FIS was designed to perform an all-sky survey in the far-infrared region with higher spatial resolution and higher sensitivity than the IRAS. A combination of the Infrared Camera (IRC) (Onaka et al. 2007) on the AKARI satellite also enables a wider wavelength coverage than IRAS.

The *Spitzer Space Telescope* (SST) (Werner et al. 2004), which is used extensively in the observation of various objects in the infrared region, has brought new insights into the universe with its high spatial resolution and high sensitivity. FIS is a complementary instrument because of its capability of covering wide areas, and its multiple photometric bands. Furthermore, the FIS has the advantage of allowing far-infrared spectroscopy with a Fourier transform spectrometer (FTS). The *Infrared Space Observatory* (ISO) (Kessler et al. 1996) demonstrated the potential of spectroscopy in the infrared region for diagnostics of the interstellar medium and radiation field. Adopting two-dimensional array detectors, the FTS of FIS works as an imaging FTS. Consequently, it affords high efficiency observations of the spatial structure in spectra.

This paper describes the design and operation of FIS in two sections, and then discusses its flight performance and advantage.

## 2. Instrument Design

The FIS is a composite instrument, consisting of a scanner and a spectrometer. Adopting the newly developed large format array detectors, FIS achieves high spatial resolution and sensitivity. Fig.1 shows a picture of FIS during final integration; the top cover is removed to show the interior.

---

* AKARI is a JAXA project with the participation of ESA

† Present Address is Japan Science and Technology Agency, 4-1-8 Honcho, Kawaguchi, Saitama 332-0012, Japan

### *2.1. Optical Design*

Fig.2 illustrates the FIS optical design. FIS is about 50 cm along the major axis and weighs about 5.5 kg. To reduce the size and resources required, the scanner and spectrometer share some optical components and detector units. Rotating the filter wheel selects the appropriate function.

Light coming from the telescope is focused near the FIS input aperture. After passing through the input aperture, the beam is bent into the FIS optical plane and led to the collimator mirror. The collimated beam goes to the filter wheel, which selects the scanner or the spectrometer by choosing the filter combination. In the scanner mode, it selects a the combination of an open hole and a dichroic beam splitter. The beam passes through the hole, and is reflected by a flat mirror to the dichroic filter on the filter wheel. Longer wavelength photons ($> 110\ \mu$m) pass through the filter and shorter wavelength photons are reflected. Camera optics focus the beams onto the detector units according to their wavelength.

A Fourier transform spectrometer (FTS) serves as the spectroscopic component. A polarizing Michelson interferometer, the so-called Martin–Puplett interferometer (Martin and Puplett 1969), is employed in the FTS optics. This type of interferometer requires input and output polarizers to provide linear polarization. These two polarizers are on the filter wheel, and are selected in the spectrometer mode. The collimated beam is reflected by the input polarizer to the interferometer, while the remaining component is absorbed by a blocking wall. A beam splitter divides the linearly polarized beam into two beams. The beam splitter is also a polarizer, whose polarizing angle is rotated by 45 degrees relative to the incident linear polarized beam. All polarizers are wire-grid filters printed on thin Mylar films supplied by QMC Instruments Ltd. The divided beams are reflected by roof-top mirrors; one is fixed and the other is movable to change the optical path difference between two beams. After that, the beam splitter recombines the two beams, and the interfered beam goes to the output polarizer. Finally, the elliptically polarized beam is separated into two axis components by the output polarizer. Each component is focused on the corresponding detector unit.

FIS has a cold shutter at the input aperture to allow measurement of the dark current of the detector. For the calibration of the detectors, there are three light sources in the FIS housing. One is in the light path of the scanner, and the others irradiate the front of each detector. The intensity and emitting duration of each lamp are independently controlled by commands independently. These lamps can also simulate the light curve of the point source in the all-sky survey. Since the simulated light curve is quite stable and reproducible, the detector responses to a point source can be monitored at any time. In addition to these calibration lamps, there is a blackbody source, whose temperature is controllable up to 40K, opposite the interferometer input that is used to check that operation of the FTS. Furthermore, to improve the transient response of the long wavelength detector, a background light source, with controllable power, is placed on the detector unit to continuously irradiate detector pixels.

At the current setting, the incident power corresponds to a sky brightness of ∼100 MJy/sr.

### *2.2. Instrumentation Description*

#### *2.2.1. Field-of-View*

We use two types of photoconductive detector array to cover the far-infrared wavelengths (50 – 180 $\mu$m). One is the direct-hybrid monolithic Ge:Ga array (Fujiwara et al. 2003) for the shorter wavelength of 50 to 110 $\mu$m (labeled SW), which was developed by the National Institute of Information and Communications Technology (NICT). The Ge:Ga monolithic array is bump-bonded by Indium with Silicon-based cryogenic readout electronics (Nagata et al. 2004). The other is a compact stressed Ge:Ga array for longer wavelengths of 110 to 180 $\mu$m (labeled LW), which is an evolved version of a previous model (Doi et al. 2002). The LW detector also employs cryogenic readout electronics. All Ge:Ga chips were supplied by NICT.

There are two arrays in each detector unit for the different photometric bands — WIDE-S and N60 for the SW detector and WIDE-L and N160 for the LW detector. The array formats are $3 \times 20$, $2 \times 20$, $3 \times 15$, and $2 \times 15$ for WIDE-S, N60, WIDE-L, and N160, respectively, as shown in Fig.3. Several pixels did not work properly after fabrication (shown by hatching in the figure); however, no additional bad pixels appeared after the launch.

The fields-of-view (FOVs) of WIDE-S and WIDE-L, N60 and N160 detectors overlap, although their coverage differs. The pixel scales are designed to be comparable to the telescope's diffraction limits. The arrays are rotated by 26.5 degrees relative to the scanning direction. Because of this configuration, the width of the stripe swept out on the sky is reduced to about 90% of the array width, although the spatial sampling grid becomes half of the pixel pitch in the cross-scan direction.

The FOVs of the SW and LW detectors were measured in space by observing point sources. The measured FOVs are shifted from the designed position by about 1 arcmin in both in-scan and cross-scan directions referred to the telescope's boresight (see top panel of Fig.3). In the spectrometer mode (bottom panel of Fig.3), the misalignment of each array is larger than in the scanner mode, which limits the observational efficiency of spectral mapping.

The distortion of the FOVs due to the FIS optics is evaluated by optical simulation. Although the actual distortion and magnification factor of the FIS optics do not match precisely, no significant discrepancy with the design is indicated.

#### *2.2.2. System Spectral Response*

The four photometric bands of FIS are defined by the combination of the optical filters and the spectral response of the detectors, as the incident photons reach the detectors through the optical filters. The collimated beam passes through two blocking filters that block the mid- and near-infrared photons contributed mainly by stars. The dichroic filter then divides the beam in the frequency domain: higher frequency photons ($> 91$ cm$^{-1}$ in wavenumber) are reflected and lower frequency photons are transmitted. Finally, two filters on the front of

each detector shape the photometric bands. Four photometric bands cover the 50 to 180 $\mu$m wavelength region; two are wide bands (WIDE-S and WIDE-L) and the other two are narrow (N60 and N160).

In the spectrometer mode, the dichroic beam splitter is replaced by a combination of three polarizers. The other optical filters are the same as for the scanner mode. Only the wide bands (WIDE-S and WIDE-L) are used for spectroscopy. The spectrometer could in principle take interferograms with narrow bands, although some of the outer pixels of the arrays will vignette the telescope beam.

Fig.4 shows the FIS system's spectral response in the photometric mode. The responses are normalized at the peak. The filters and optics were measured in an end-to-end system configuration at room temperature, although the narrow band filters for N60 and N160 were measured individually at cryogenic temperature, since their properties depend on temperature.

The spectral responses of the detectors were evaluated by a spectrometer, each pixel of the detector array having a different spectral response. This difference is larger in the LW detector, due to non-uniformity of the effective stress on the Ge:Ga chips. The plot in Fig.4 provides typical profiles. The spectral response of each pixel must be used to calculate precise pixel-to-pixel color corrections.

The spectral response can also be measured by the FIS spectrometer itself, using the internal and external blackbody sources at different temperatures. In orbit, we confirmed the system spectral response of FIS in this manner. The spectra of the internal blackbody source taken in orbit are within 10% of those measured in the laboratory after scaling the responsivity. Since the filters and optics are considered stable, the system spectral response of each photometric band is expected to be similar to that measured in the laboratory as shown in Fig.4.

The blocking filters are expected to avoid leakage of the mid- and near-infrared photons. The blocking efficiency required from the scientific observations is $10^{-5}$ at 10 $\mu$m and $10^{-9}$ at 0.5 $\mu$m, which are realized optimally, and will in future be checked by observations of well-known stars.

## 3. Observation Modes

### *3.1. All-Sky Survey*

FIS is designed primarily to perform an all-sky survey with four photometric bands. The goal is to observe the entire sky for at least two independent orbits. The first half year following the performance verification phase is dedicated to observations for the all-sky survey. During the remaining life, supplemental survey observations will fill in the incomplete sky areas, sharing the observation time with dedicated science programs.

During the survey, the detectors are read out continuously with a constant sampling

rate for each array, corresponding to about three samples in a pixel crossing time. Detectors are reset to discharge the photo current at appropriate intervals of about 2 sec nominally, 0.5 sec for bright sky, and for each sampling (correlated double sampling: CDS) at the Galactic plane, whose reset intervals correspond to about 26 and 45 ms for the SW and LW detectors, respectively. Calibration flashes with illuminator lamps are inserted periodically every minute while keeping the shutter open to trace the detector responsivity. Near the ecliptic poles, where the detectors sweep frequently, a one-minute calibration sequence with the shutter closed is executed for nearly every orbit to monitor the long term trend of the detector responsivity.

### *3.2. Pointing Observation*

Before launch of the AKARI satellite, the project science team members selected the core programs and target sources were selected. In addition to the core programs, some portion of the observation time was open to the community. For the scientific programs and the Open Time proposals, the AKARI instruments operate in a pointing mode. The FIS observations are categorized in three major astronomical observation templates (AOTs), — two for photometry and one for spectroscopy. Details of each AOT are described below.

#### *3.2.1. FIS01: Compact Source Photometry*

The FIS01 template is used to observe point-like or small scale sources. In this AOT, for one pointing observation, the detectors sweep the sky two times in round trips. Between two round trips, the scan path is shifted by either a few pixels (70 arcsec) or half of the FOV (240 arcsec) in the cross-scan direction, which is selectable. The other adjustable parameters are the reset interval and scan speed. The scan speed is selectable from 8”/sec or 15”/sec, which are nearly 14 to 30 times slower than that of the all-sky survey. The detection limits should be improved by a factor of the exposure time or more using the charge integration amplifier. Furthermore, using a slower scanning speed reduces the transient response effects of the detector response.

An observation sequence takes about 30 minutes as shown in the top panel of Fig.5. During about 10 minutes of maneuvering to the spacecraft to point toward the target, the standard calibration sequence is executed with the shutter closed, i.e., measuring dark current, illuminating the calibration lamps continuously for about two min and flashing the calibration lamps several times. After opening the shutter and waiting 210 sec, the scanning sequence begins and continues for about 12 minutes. Then, the shutter is closed again and the maneuver to the all-sky survey begins with the post observation calibrations. During scanning observations, at the scan turning points, the shutter is closed for 30 sec and the calibration lamps are turned on for about eight sec to monitor the drift of the detector responsivity during the pointing observation.

*3.2.2. FIS02: Wide Area Mapping*

FIS02 is the template for wide area mapping. This AOT executes only one round trip. The detectors sweep a longer strip than for FIS01, but the detection redundancy is reduced. Overlapping scans are critical for high quality wide area mapping. By selecting the 15"/sec scan speed, the strip length reaches over one degree. The calibration sequences in the pre- and post observation phase and at the turning point are the same as for FIS01. The middle panel of Fig.5 illustrates the observation sequence.

*3.2.3. FIS03: Imaging Spectroscopy*

FIS03 is the template for spectroscopic observations. The bottom panel of Fig.5 illustrates the observation sequence. In this AOT, the target is locked on the detectors. To use the FTS, the optics are switched to FTS mode by rotating the filter wheel during the maneuver to the target position. The sampling sequence changes for the FTS and the movable mirror starts to operate. Important parameters in FIS03 are the spectral resolution and array selection. Users choose from two spectral resolution modes: a full resolution mode and a low resolution mode (named SED mode), with spectral resolution of 0.19 $cm^{-1}$ and 1.2 $cm^{-1}$ without apodization, respectively. Taking one interferogram in the full resolution mode takes four times longer than that in the SED mode. Consequently, in one pointing observation, 15 full resolution or 59 SED mode interferograms can be taken. The other important parameter is the array selection, which was added after launch, because the FOVs of the two detectors are misaligned as shown in Fig.3. Depending on the position of the target on the detectors, there are three choices: nominal, SW, and LW positions.

During the maneuver to the target position, the internal blackbody source is turned on at the proper temperature, with the shutter closed, and interferograms are taken as reference spectra. A short calibration sequence using the calibration lamps is also conducted at the pre- and post observation phase. After the observation, the observation mode changes to photometry mode for the all-sky survey, during the recovery maneuver to the all-sky survey.

Parameters for each AOT are summarized in Table 1.

*3.2.4. Parallel Observation*

FIS can operate in parallel with the IRC observations. Since the FOVs of FIS are separated from the FOVs of the IRC by about half a degree, they can not observe the same target. Nevertheless, taking data with FIS is interesting in many cases as a serendipitous survey. The nominal operation of the IRC is to make observations with long exposure times to provide deep images or spectra. Since the FIS photometry is designed for scanning mode, the pointed observations of the photometry are ineffective due to the narrow array formats and larger pixel scales. Therefore, FIS is operated in the spectrometer mode, if the sky is bright enough to detect signals by the FTS. The observation sequence for parallel observation is the same as for FIS03. These parallel observations are productive, especially for the Large Magellanic Cloud,

where IRC is making systematic surveys, as well as toward bright complex regions like the Galactic plane.

Specific calibration sequences operates during the remaining IRC oriented observations. Once a day, the calibration sequence to evaluate detector transient response is executed. About once every three days, the calibration lamp stability is also measured. These calibration data are used to track long term trends in detector performance.

## 4. Flight Performance

In orbit, all FIS functions are working as designed. The cold shutter and the filter wheel have operated constantly while in orbit, more than ten thousand times and a few hundred times, respectively. All the functions are controlled by the onboard electronics without any difficulty. In the following subsections, the FIS flight performance is described.

### *4.1. Imaging Quality*

The point spread functions (PSFs) of FIS were measured in the laboratory using a pin hole source. Widths of the measured PSFs were almost consistent with those expected from the optical simulation. In orbit, the system PSFs including the telescope system are constructed from observations of bright point sources. The PSFs are similar to the laboratory measurements. As shown in Fig.6, the PSFs conform to the estimations from the optical model at more than the half maximum of the peak. The full widths at the half maximum of the PSFs, derived from Gaussian fitting, are summarized in Table 2. At the tails of the PSFs, there are significant enhancements, whose power is about 30% of the total power. This extended halo is a cause for the degradation of source detection.

In the spectrometer mode, the PSFs are evaluated by slow scan observations of the point sources with the spectrometer optics, and are about 20% wider than in the photometer mode. It is, however, possible to take spectra for each pixel and images with nearly one arc minute spatial resolution, simultaneously.

An additional factor degrades the imaging quality of the SW detector, namely, considerable cross talk between pixels in both axes of the arrays. One possibility to explain this phenomenon is that the incident far-infrared photons diffuse into the monolithic Ge:Ga array during multiple reflection on the front and back surfaces of the detector substrate. Furthermore, both the SW and the LW detectors show significant ghost signals. The reason for the ghost is, presumably, electrical cross talk in the multiplexer of the cryogenic readout electronics. In this case, the ghost appears in other arrays of the same detector. The images of the asteroid *Ceres* observed by FIS01 are shown in Fig.7, as an example. To enhance the effect of the cross talk, the color level has been adjusted. Since the position and strength of the cross talk are stable, it should be possible to remove it from the original.

Another possible degradation of the image quality comes from the detector's transient

response. For pointed observations, the detector scans a source, both forward and backward on the same pixel. The effect of transient response has been evaluated for each observation, and is not significant for slow scan observations.

### *4.2. Detector Performance*

The readout method for the FIS detectors is based on a Capacitive Trans-Impedance Amplifier (CTIA) using newly developed cryogenic devices (Nagata et al. 2004). Although the CTIA has a wide dynamic range, the linearity is rather poor, and the effective bias on the detectors drifts. In laboratory measurements, the relation between the output signal and the amount of the stored charge was well calibrated, and the relation is confirmed in orbit. Therefore, the photo current can be accurately reproduced from the output signal.

Charged particle hits are another important influence on detector performance. About once a minute, charged particles hit a pixel, and in some cases, the responsivity drifts for between several seconds and several minutes. Near the South Atlantic Anomaly (SAA), the hit rate of charged particles is too high to observe the sky signal. After passing the SAA region, the detector responsivity increases significantly and relaxes gradually with a decay on the order of hours. To cure the effect of the SAA, bias boosting is applied just after passing through the SAA. By increasing the bias voltage to breakdown for a short time, the detector responsivity quickly relaxes to a stable level.

Finally, the pixel-to-pixel variations of the detector responsivity are shown in Fig.8, which are the relative detector signals in the observation of flat sky. The unevenness of the detector responsivity could come from the non-uniformity of the effective detector bias, due to the offset of the readout electronics. This is particularly an issue for the LW detector, because of its small bias voltage. In addition, due to variations of the spectral response for each pixel in the LW detector, it has poor flatness as compared to the SW detector.

### *4.3. Photometric Calibration*

For absolute calibration, several kinds of astronomical sources are used — well-modeled objects such as asteroids, planets, stars and galaxies, as well as the spectra of bright IR cirrus or interplanetary dust emission. To calibrate the absolute flux from point like sources, the aperture photometry procedure must be defined, and then applied to the observations of asteroids, stars and galaxies with a wide range of fluxes. The relation between the signal and the source flux for several sources has a good linear correlation as shown in Fig.9. The uncertainties of the current signal to flux calibration are no more than 20% for the N60 and WIDE-S bands, and 30% and 40% for the WIDE-L and N160, respectively. Our goal is to reach an absolute calibration accuracy of about 10% in all bands. We will achieve this by mitigation of various image artifacts described in this paper, and through analyses of many repeated observations of our network of well-known calibration sources, that are performed continually.

Comparing the signals of the sky brightness measured by FIS and DIRBE on COBE,

which provide a well calibrated infrared sky map, we can obtain the absolute calibration for sky brightness. The observations of bright IR cirrus regions with no significant small scale structure are compared with values measured by DIRBE to make an absolute calibration. The resulting calibration, however, disagrees with the calibration derived from the point like sources by a factor of about two. The absolute calibration for diffuse sources still has a large uncertainty due to the difficulty of baseline estimation. Furthermore, the contribution of detector transient response differs between the two calibration methods.

According to the absolute calibration derived from the compact sources, the nominal detection limits evaluated from the signal-to-noise ratio of the detected sources are listed in Table 2. The performance of the pointed observation is demonstrated by Matsuura et al. (2007).

### *4.4. Spectroscopic Performance*

All the spectrometer functions work as they did in the laboratory. After tuning the control sequence of the movable mirror, interferograms of the internal blackbody source and sky were measured. The Fourier transformed spectra of the internal blackbody source are consistent with that taken in the laboratory, within a 10% error after scaling the responsivity, which means that the laboratory optical performance is reproduced in space.

The data reduction to reproduce source spectra is difficult because the interferogram is distorted by the detector transient response as described above. Furthermore, a channel fringe in the interferogram also causes complications. Through observations of well-known bright sources, line sensitivity and reproducibility of spectra were evaluated. The FTS system performance is almost same as the estimates from the laboratory measurements. The line spectrum observed by the FTS is shown in the Fig.10 as an example. The spectral resolution of the FTS in full resolution mode is about 0.19 $\mathrm{cm}^{-1}$, which agrees well with the expected value of 0.185 $\mathrm{cm}^{-1}$. Interim detection limits of the FTS derived for on-source pixels from observations of bright sources are roughly 20 Jy, 50 Jy and 100 Jy for continuum spectra in wavenumber of $65-85$ $\mathrm{cm}^{-1}$, $90-120$ $\mathrm{cm}^{-1}$ and $>120$ $\mathrm{cm}^{-1}$, respectively, and, $3\times10^{-15}$ $Wm^{-2}$ and $5\times10^{-14}$ $Wm^{-2}$ for line emissions of [CII](158 $\mu$m) and [OIII](88 $\mu$m), respectively, which are $5\sigma$ values for one-pointed observation.

### *4.5. Comparison with Other Instruments*

FIS strives to provide an improved version of the all-sky survey performed by IRAS more than two decades ago. The spectral coverage of FIS is extended to longer wavelength by the WIDE-L and N160 bands, which cover up to 180 $\mu$m. The longer wavelength coverage allows determination of the contribution of cold dust components, which perform important roles in the interaction of the interstellar medium and radiation field. The advantage of longer wavelength capability has been demonstrated by the ISOPHOT Serendipity Survey (ISOSS) of ISO (Stickel et al. 2007b). Although the sky coverage of ISOSS is about 15% of the whole sky, the ISOSS 170 $\mu$m Sky Atlas is utilized in variety of fields, especially, related to galaxies

and cold galactic sources. This precursor survey indicates the benefit of the longer wavelength bands in the FIS all-sky survey. The high spatial resolution of the FIS all-sky survey is a great advantage for source detection and detailed mapping. As shown in above, the spatial resolution of the FIS, which is about 0.7 acrmin for the N60 and WIDE-S bands, and about 1 arcmin for the WIDE-L and N160 bands, is more than five times better than IRAS even in the longer wavelength bands. The higher spatial resolution comes from the progress of detector technology, although the 60 cm diameter telescope of IRAS is comparable with the AKARI telescope (Kaneda et al. 2007a). These advantages of the FIS all-sky survey are demonstrated by Jeong et al. (2007) and Doi et al. (2007).

The point source flux levels at signal-to-noise ratio of five for one scan are listed in Table 2. We processed the observed data using the preliminary version of the data-processing pipeline for the all-sky survey data. We estimated the system sensitivity based on a series of observations of asteroids as calibration sources in the all-sky survey. We used Sussextractor, which is a point source extraction and photometry software dedicated for the AKARI all-sky survey (Savage et al. 2007), to make the photometry of the asteroids. We derived noise levels by observing dark areas of the sky. The estimated flux levels are significantly degraded from the detection limits estimated prior to the launch (see Table 3 in Matsuhara et al. 2006). We found several causes for the degradation. Firstly, we observed several types of excess noise in orbit. The current version of the pipeline successfully removed the effects of some types of noises. Secondly, we also observe the response to point sources is smaller than we expected. This is partly due to the PSFs described above, and partly due to the detector AC response. Thirdly, we reduced the bias voltage for Wide-L and N160 in orbit to stabilize the behaviour of detectors after irradiation of high-energy particles. Furthermore, the actual source detection is degraded by various effects, e.g. frequent glitches due to high energy particles and low-frequency baseline fluctuation due to the change of the detector responsivity, in the data reduction process. The potential performance of 90 $\mu$m band (WIDE-S), however, is higher than that of the IRAS 100$\mu$m band. Unfortunately, the detection limits of the LW detector, which provides new wavelength bands, are also degraded. The potential performance of the longer wavelength bands is comparable to or better than the ISOSS. The galaxy list of ISOSS has a 170 $\mu$m completeness limit of about 2 Jy (Stickel et al. 2007a), and is useful for a cross calibration of the all-sky survey. The performance of the all-sky survey evaluated from an initial mini-survey will be discussed by Shibai et al. (2007b).

The performance of the detailed observations using the pointing observation mode should be compared with the recent instrument MIPS on SST. MIPS has advantages in spatial resolution and sensitivity, as a result of its larger telescope, small pixel scales, and long exposure capability. The advantage of FIS is that it has four photometric bands between 50 and 180 $\mu$m, whereas MIPS has only two bands (70 $\mu$m and 160 $\mu$m) in the corresponding wavelength range. Multi-band photometry with FIS is effective for determining a spectral energy distribu-

tion (Kaneda et al. 2007b; Suzuki et al. 2007). The performance of the slow scan observation is demonstrated by Matsuura et al. (2007), who reported the detection limit at 90 $\mu$m (WIDE-S) achieves 26 mJy ($3\sigma$) using the observations at the Lockman Hole. In the paper, they discuss about the source counts, and point out that the number of sources detected at 90 $\mu$m is significantly smaller at the faint end compared to the expected values from the model, which explains the MIPS source counts well. This implies that FIS is a complementary instrument to MIPS in the SED coverage. In the main observation phase, the low cirrus region near the South Ecliptic Pole (SEP) is observed by FIS intensively with almost the same sensitivity at the Lockman Hole for about 10 square degrees (Matsuhara et al. 2006). The deep survey near the SEP will become a legacy survey of FIS for extragalactic studies.

The spectroscopic capability in the far-infrared region is a unique feature of FIS in contrast to MIPS. Previously, LWS on ISO was available for far-infrared spectroscopy. The wavelength coverage and the spectral resolution of LWS in the grating mode are comparable with the FIS spectrometer. The sensitivity of FIS in the spectrometer mode is not so excellent as mention above. However, the spectrometer of FIS has the advantage of high observational efficiency. Since it is an imaging FTS, FIS can take spectra with arcminute spatial resolution. For example, FIS could map the M82 galaxy with spectra in several pointed observations, which correspond to about one hour exposure time. Furthermore, the spectroscopic serendipity survey by parallel observations is expected to provide a unique dataset.

## 5. Summary

The Far-Infrared Surveyor was designed to survey the far-infrared region with four photometric bands within 50 – 180 $\mu$m, with high spatial resolution and sensitivity. Additionally, a spectroscopic capability was installed as an imaging Fourier transform spectrometer. All functions of FIS work very well in orbit. FIS performance is demonstrated in the initial papers of this volume. The all-sky survey is performed continuously and should provide a new generation all-sky catalog in the far-infrared. In addition to the all-sky survey, a large area deep survey ($\sim$ 10 square degrees) near the South Ecliptic Pole and many scientific programs are being executed.

To bring out the potential of the FIS instrument, the data processing methods are continuously being improved. Since calibration data are accumulated constantly by the end of the mission life, the FIS data quality should be substantially better than that listed here.

The AKARI project, previously named ASTRO-F, is managed and operated by the Institute of Space and Astronautical Science (ISAS) of Japan Aerospace Exploration Agency (JAXA) in collaboration with the groups in universities and research institutes in Japan, the European Space Agency, and Korean group. We thank all the members of the AKARI/ASTRO-F project for their continuous help and support. FIS was developed in collaboration with ISAS,

Nagoya University, University of Tokyo, National Institute of Information and Communications Technology (NICT), National Astronomical Observatory of Japan (NAOJ), and other research institutes. The AKARI/FIS All-Sky Survey data are processed by the international team which consists of members from the IOSG (Imprerial College, UK, Open University, UK, University of Sussex, UK, and University of Groningen, Netherlands) Consortium, Seoul National University, Korea, and the Japanese AKARI team. The pointing reconstruction for the All-Sky Survey mode is performed by the pointing reconstruction team at European Space Astronomy Center (ESAC). We thank all the members related to FIS for their intensive efforts toward creating new frontier. M. Cohen's contribution to this paper was partially supported by a grant from the American Astronomical Society. We would like to express thanks to Dr. Raphael Moreno for providing flux models of giant planets.

## References

Doi Y., et al., 2002, Adv. in Space Research, 30, 2099
Doi Y., et al., 2007, PASJ, 00, 000
Fujiwara M., Hirao T., Kawada M., Shibai H., Matsuura S., Kaneda H., Patrashin M.A., & Nakagawa T., 2003, Appl. Opt., 42, 2166
Jeong W-S., et al., 2007, PASJ, 00, 000
Kaneda H., Kim W., Onaka T., Wada T. Ira Y., Sakon I., & Takagi T., 2007a, PASJ, 00, 000
Kaneda H., et al., 2007b, PASJ, 00, 000
Kessler M.F., et al. 1996, A&A, 315, L27
Martin D.H., & Puplett E., 1969, Infrared Phys., 10, 105
Matsuhara, H., et al., 2006, PASJ, 58, 673
Matsuura, S., et al., 2007, PASJ, 00, 000
Murakami H., et al. 2007, PASJ, 00, 000
Nagata H., Shibai H., Hirao T., Watabe T., Noda M., Hibi Y., Kawada M., & Nakagawa T., 2004, IEEE Trans. on Elec. Devices, 51, 270
Nakagawa T., et al., 2007, PASJ, 00, 0000
Onaka T., et al. 2007, PASJ, 00, 000
Savage R., et al. 2007 in preparation
Shibai H., 2007a, Adv. in Space Research, accepted for publication
Shibai H., 2007b, in preparation
Stickel, M., Klaas, U., and Lemke, D., 2007a, A&A, 466, 831
Stickel, M., Krause, O., Klaas, U., and Lemke, D., 2007b, A&A, 466, 1205
Suzuki T., Kaneda H., Nakagawa T., Makiuti S., Doi Y., & Shibai H., 2007, PASJ, 00, 000
Werner M.W., et al. 2004, ApJS, 154, 1

**Table 1.** Parameters of FIS AOTs

| **AOT** | **FIS01** | **FIS02** | **FIS03** |
|---|---|---|---|
| observation mode | slow scan | | pointing |
| observation target | compact source | area mapping | spectroscopy |
| **parameters:** | | | |
| - target position | center of scan area | | source |
| - reset interval* | [CDS, 0.25 s, 0.5 s, 1.0 s, 2.0 s] | | [0.1 s, 0.25 s, 0.5 s, 1.0 s, (2.0 s)] |
| - parameter 1* | scan speed | | spectral resolution |
| | [8"/s, 15"/s, (30"/s)] | | [full res., SED] |
| - parameter 2 | shift size | - | array selection |
| | [70", 240"] | - | [MOD, SW, LW] |
| amount of data† | 17.5 MB | | 49.8 MB |

Notes.

* Parenthetic values of parameters are option.

† Data size that FIS generates in one pointing observation.

**Fig. 1.** A picture of FIS at final integration. The top cover is removed to show the FIS optics. The orientation of the FIS is the same as in Fig.2

**Table 2.** Flight Performance of FIS

| **BAND** | **N60** | **WIDE-S** | **WIDE-L** | **N160** | |
|---|---|---|---|---|---|
| band center | 65 | 90 | 140 | 160 | [$\mu$m] |
| effective band width* | 21.7 | 37.9 | 52.4 | 34.1 | [$\mu$m] |
| pixel scale | 26.8 | 26.8 | 44.2 | 44.2 | [arcsec] |
| pixel pitch | 29.5 | 29.5 | 49.1 | 49.1 | [arcsec] |
| **point spread functions:** | | | | | |
| - measured FWHM† | 37 ± 1 | 39 ± 1 | 58 ± 3 | 61 ± 4 | [arcsec] |
| **flat field:** | | | | | |
| - variation‡ | 19% | 14% | 43% | 53% | |
| $5\sigma$ **flux level:** | | | | | |
| - survey mode$ | 2.4 | 0.55 | 1.4 | 6.3 | [Jy] |
| - pointing mode‖ | 110 | 34 | 350 | 1350 | [mJy] |

Notes.

* Effective band width for the given band center under the assumption of $\nu F_\nu = const.$

† FWHM derived from Gaussian fitting of PSFs constructed from observations of asteroids in the photometer mode.

‡ Relative variations (standard deviations) to the averages for each array.

$ Point source flux level with signal-to-noise ratio of 5 for one scan in the all-sky survey mode.

‖ Point source flux level for one-pointed observation by FIS01 with 8"/sec scan speed and 2 sec integration time, which include both detector and source noises.

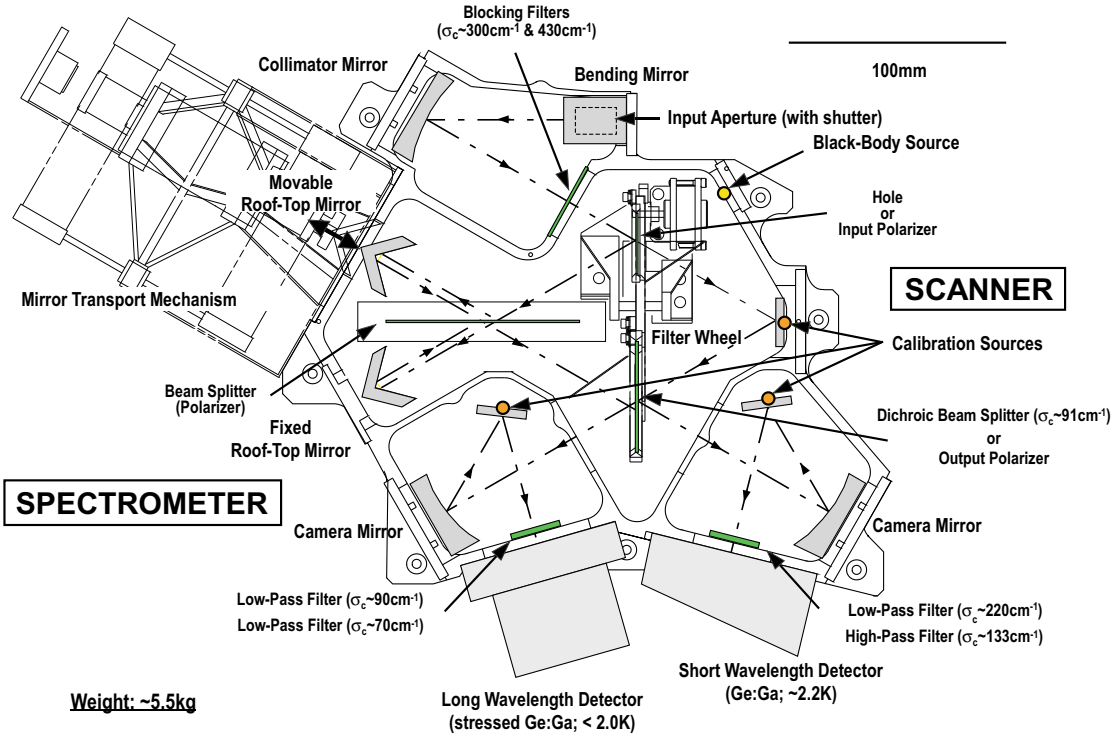


**Fig. 2.** Drawings of the FIS optical configuration. The major optical components are shown with labels. The FIS instrument provides two functions — the scanner (left side) and the spectrometer (right side), which use different optical paths. Each function is selected by rotating the filter wheel.

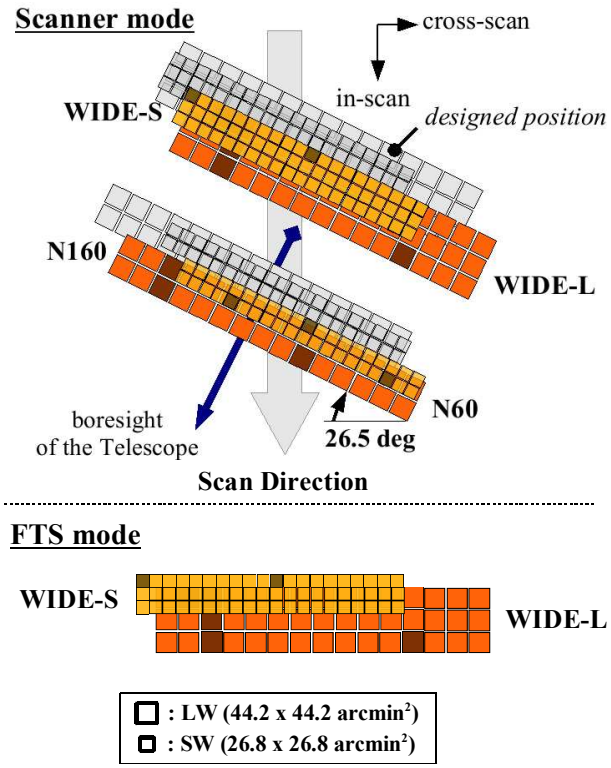


**Fig. 3.** Details of the FOVs of FIS. The upper panel shows the FOVs in the scanner mode. The FOVs measured in orbit are drawn on the designed FOVs with light gray. The detector's field-of-views are shifted from the designed location, which is referred to the boresight of the telescope. The misalignments of each array are about one pixel. The major axis of the arrays is rotated by 26.5 degrees in the scan direction to improve the grid pitch in the cross-scan direction. The lower panel shows FOVs in the spectrometer mode, in which WIDE-S and WIDE-L are active. The misalignment of each array is larger than in the scanner mode. The accuracy of the measured alignment is about half of a pixel size. Inactive pixels are indicated by hatching.

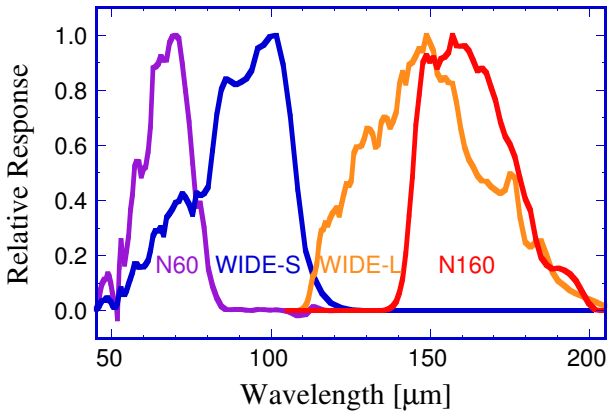


**Fig. 4.** Plots of the system spectral responses of the FIS photometric bands. These shapes are obtained from spectral measurements of optical components and detectors. The achieved optical efficiency is nearly 50% for all bands, except N60. This plot is typical, however, pixel-to-pixel variation can be seen.

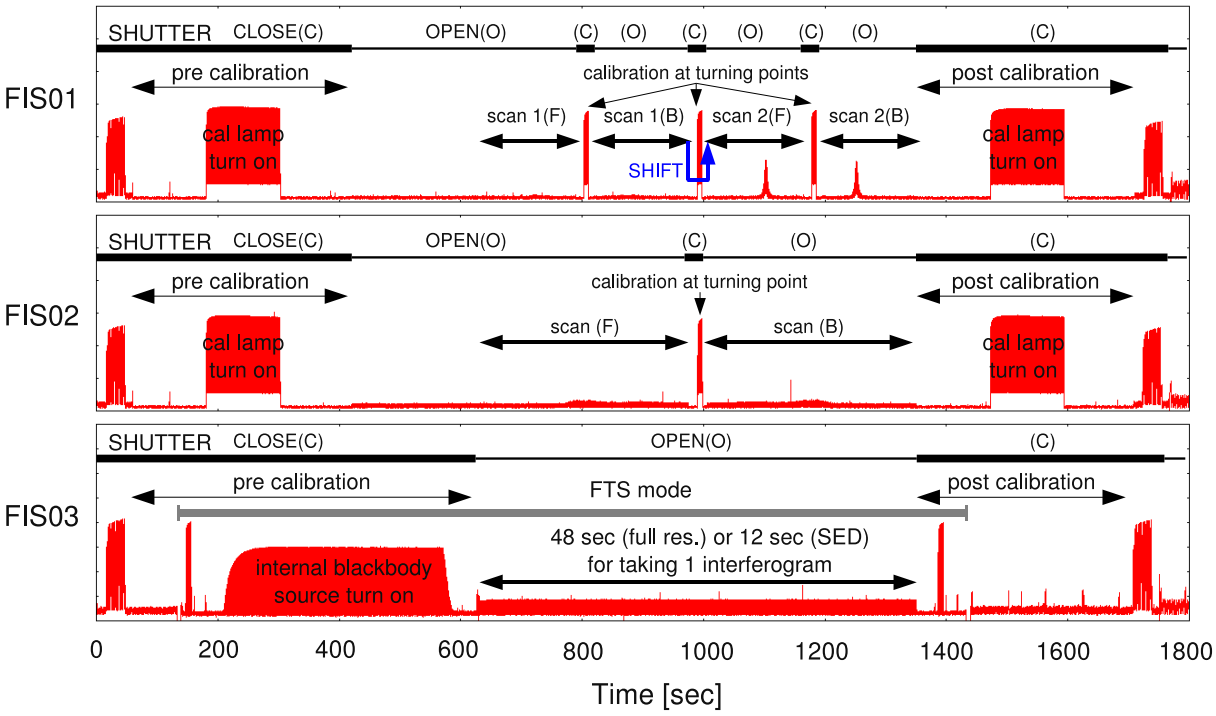


**Fig. 5.** Observation sequences of each AOT are illustrated on the real signal of the SW detector. The top panel shows the sequence for FIS01, which has two round trips with different offsets to the target position in the cross-scan direction. The middle panel is for FIS02, which has one round trip. In pre- and post-calibration, calibration lamps are turned on for two minutes with the shutter closed. At the turning points, calibration lamps are illuminated for about eight seconds with the shutter closed. The bottom panel indicate the sequence of FIS03, which is for spectroscopy. During pre calibration, the internal blackbody source is activated, and the reference spectra are taken for about six minutes. In the following 12 minutes, sky spectra are observed continuously. Signals before pre-calibration and after post-calibration are the one-minute calibration for the all-sky survey.

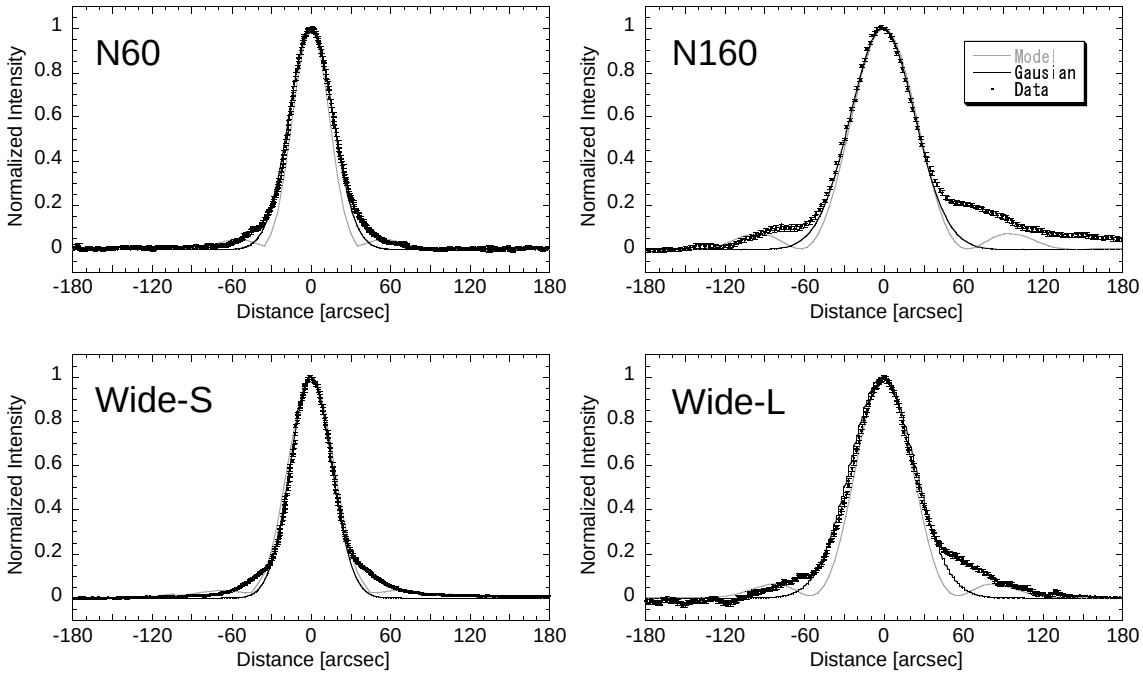


**Fig. 6.** The PSF for each band constructed from the observations of asteroids (data points) with the Gaussian fit (thin line) at the central part. Expected PSFs from the optical model are indicated by dotted lines. There are significant enhancement at the tails of the PSFs in all bands.

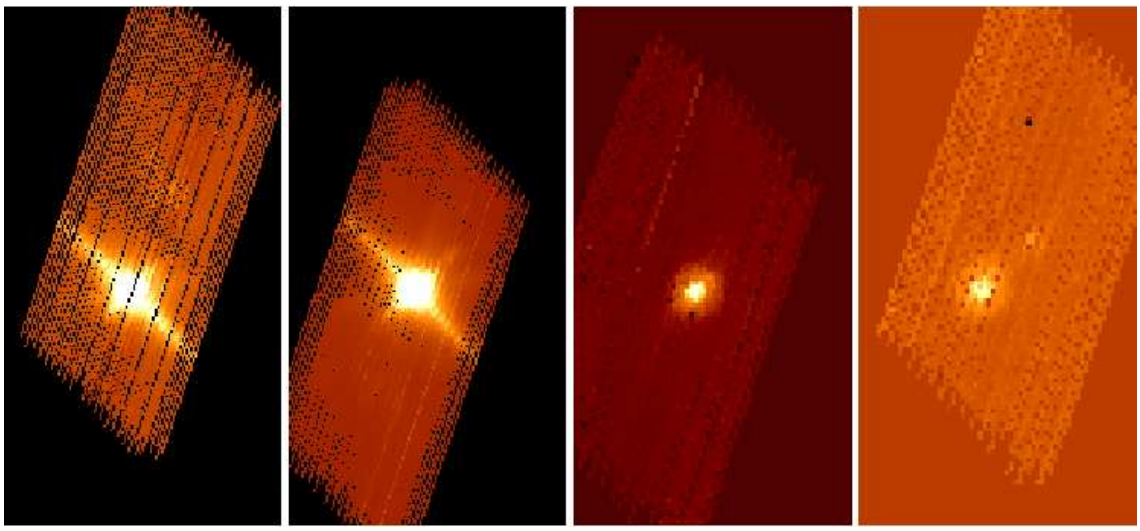

**Fig. 7.** A demonstration of the imaging quality of FIS. The raw image of the asteroid *Ceres* for each band is shown in each panel, observed by FIS01. The panels are N60, WIDE-S, WIDE-L, and N160 (from left to right). The color scale is modified to enhance the lower signal level. The ghost signals are seen in all bands, especially for narrow bands. In the images of the SW detector, cross talk signal is clearly seen along both array axes.

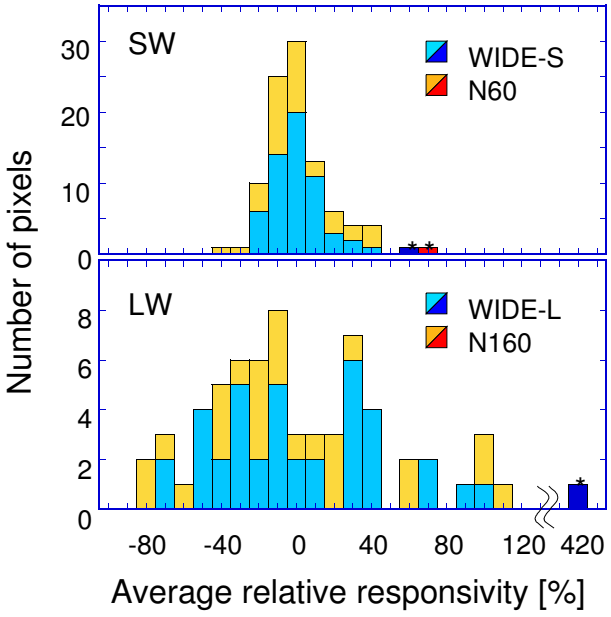


**Fig. 8.** The histogram of the pixel variation for relative responsivity. The horizontal axis is normalized by the mean value for each array excluding the anomalously high responsivity pixels, which are marked by asterisks in the figure. The variation in the LW detector is larger than in the SW detector.

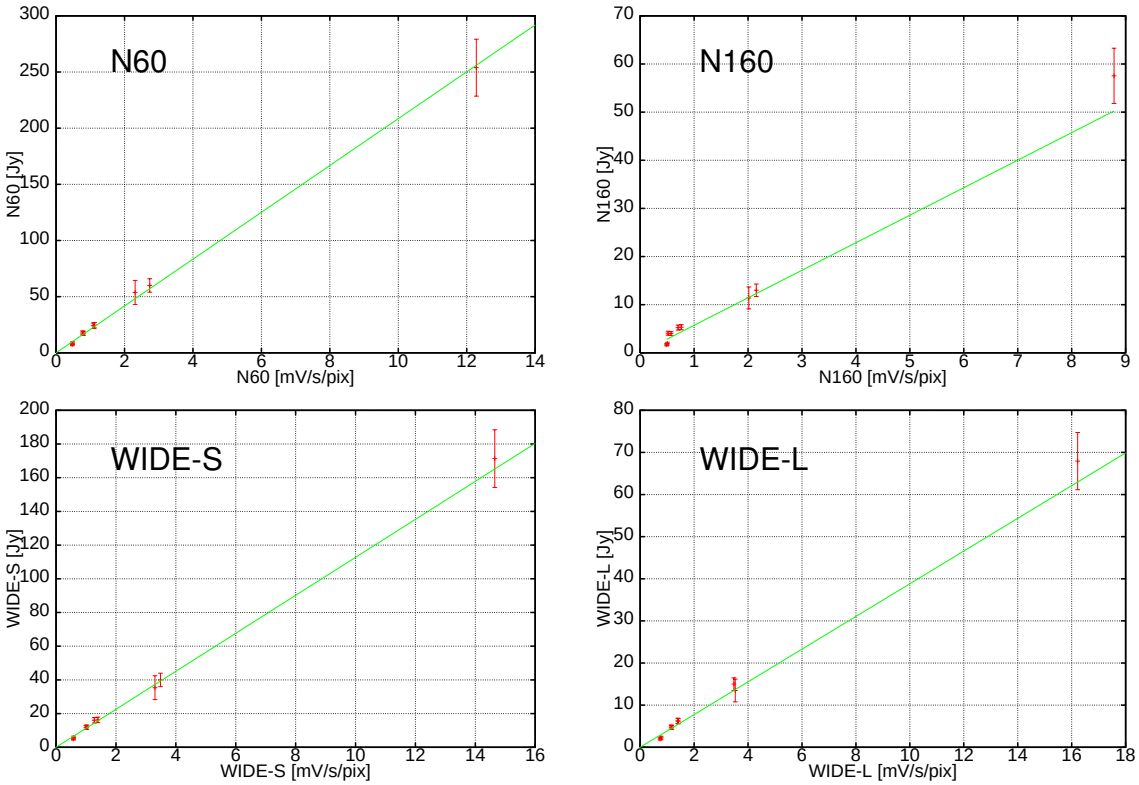


**Fig. 9.** The relation between the output signal and the model flux of point sources for each band, observed in the pointing mode by FIS01. The output signal is the integrated power within the definite aperture size, and is corrected by the calibration lamps. Clear linear relations between the source flux and the output signal are seen in all bands for more than one order of magnitude in flux range.

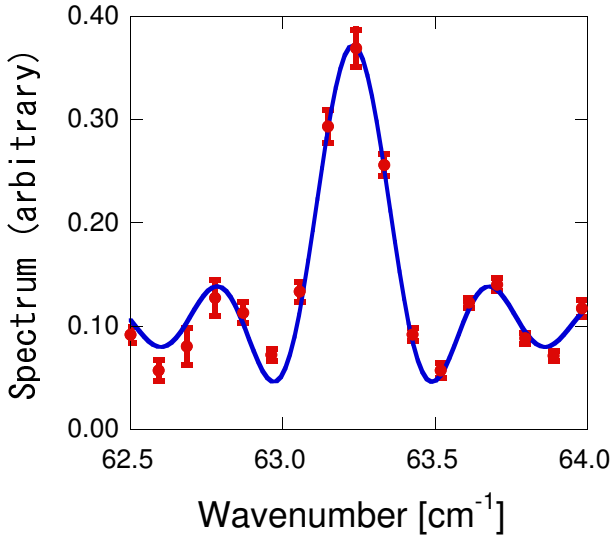


**Fig. 10.** A line shape detected by the FTS. This plot is a close up around the [CII](157.74 $\mu$m) line observed in M82. Filled circles with error bars are the measured spectrum without apodization in arbitrary units. The line is the best fit curve using a sinc function. The derived spectral resolution from the fitting is about 0.19 cm$^{-1}$, which is consistent with the expected resolution of 0.185 cm$^{-1}$.